29th Congress of the International Council of the Aeronautical Sciences
St. Petersburg, Russia; September 7-12, 2014

QUASI-ANALYTICAL AERODYNAMIC METHODS FOR PROPULSIVE FUSELAGE CONCEPTS

Sascha Kaiser*, Richard Grenon, Julian Bijewitz*, Alexander Prendinger*, Olivier Atinault**, Askin T. Isikveren*, Mirko Hornung***
***Bauhaus Luftfahrt e.V. Munich, Germany, **ONERA, The French Aerospace Lab**

Keywords: *Propulsive Fuselage, Boundary Layer Ingestion, Aerodynamics*

Abstract

A shift in aircraft design paradigm is motivated by taking synergy effects of the airframe and propulsion system integration into account. A source of power saving not utilized in contemporary aircraft lies in the ingestion of the airframe-borne boundary layer by the propulsion system. A particularly beneficial arrangement has been identified in the architecture of the so-called Propulsive Fuselage, realized by a large fan rotating around the aft fuselage. A newly developed quasi-analytical aerodynamic method has been verified and compared to Computational Fluid Dynamics (CFD) results. It has demonstrated reasonable results compared to CFD calculations for a configuration like the Propulsive Fuselage. In order to increase applicability of the quasi-analytical methods in exploring the design space, the implementation of other propulsor configurations is necessary. This includes ducted fans and two-stage configurations, i.e. counter-rotating propellers and ducted counter-rotating fans.

Nomenclature

Symbol	Description	Unit
A^+	Empirical turbulence constant	-
B	Number of blades	-
c_p	Pressure coefficient	-
$\bar{c_p}$	Specific heat	-
D	Drag	N
D_p	Pressure drag	N
D_f	Friction drag	N
F	Tip correction factor	-
H	Total specific enthalpy	J/kg
l_m	Mixing length	m
L	Fuselage length	m
$\dot{m}$	Mass flow	kg/s
M	Mach number	-
p	Pressure	Pa
Δp	Pressure gradient across the propulsor	Pa
P	Propulsor power required	W
PSC	Power Saving Coefficient	-
q	Source distribution	m^2/s
Q	Source strength	m^3/s
R_{tip}	Radial distance of blade tips to x axis	m
R	Radius of the fuselage	m
R_g	Specific gas constant	J/kg/K
r	radial coordinate	m
s	Arc length coordinate	m
T	Gross thrust of propulsor	N
T_N	Net thrust of Propulsive-Fuselage	N
U_∞	Free stream velocity	m/s
U	Velocity component in x direction	m/s
V	Velocity component in y direction	m/s
w	Radial work ratio	-
x, y, z	Coordinates in body and streamline direction	m
x_0	x coordinate of a source	m
x^*	Distance from the propulsor plane	m
y	Wall normal coordinate	m
y^+	Normalized wall normal coordinate	-
$(\cdot)'$	Equivalent inviscid parameter according to Prandtl-Glauert-Ackeret	-

δ	Boundary layer displacement thickness	m
δ_{99}	Boundary layer thickness	m
η_{pr}	Propulsive Efficiency	-
θ	Momentum loss thickness	m
θ^*	Energy loss thickness	m
κ	Empirical turbulence constant	-
ν	Kinematic viscosity	m^2/s
ν_t	Turbulent kinematic viscosity	m^2/s
ρ	Fluid density	kg/m^3
τ	Shear stress term	Pa
τ_0	Wall shear stress	Pa
ϕ_t	Blade tip flow angle	deg
Φ	Streamline Potential	m^2/s

1 Introduction

The concept of distributing propulsion has a long and broad history in aircraft design. The integration of the propulsion system into the airframe in order to gain synergistic benefits requires advanced interaction between design tools and sophisticated aerodynamic investigation compared to a conventional tube-and-wing design with podded engines in the freestream. The main benefits aspired through distributed propulsion are increased propulsive efficiency, powered lift and reduced thrust requirement in case of a high number of propulsive devices [1-3].

A shift in aircraft design paradigm is motivated by taking synergy effects of airframe and propulsion system integration into account [4]. A source of power saving not utilized in contemporary aircraft lies in airframe Boundary Layer Ingestion (BLI) by the propulsion system. A particularly beneficial arrangement has been identified in the architecture of the Propulsive-Fuselage [5], realized by a large fan rotating around the fuselage as depicted in Fig. 1. In order to investigate this concept, advanced aerodynamic methods are presented and applied to a fuselage geometry.

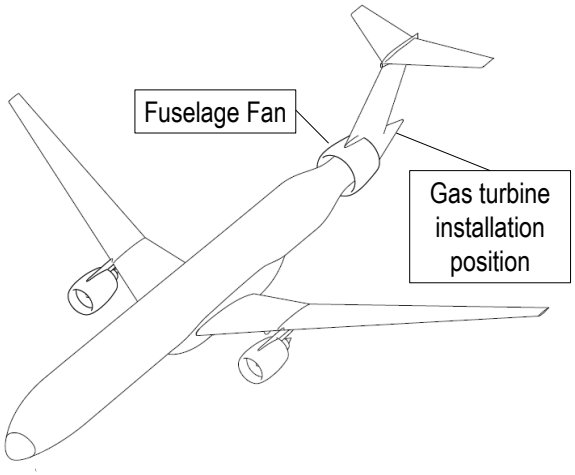

Fig. 1: Illustration of a Propulsive-Fuselage Concept with two podded engines and a Fuselage Fan at the rear [5].

The mechanism responsible for increasing propulsive efficiency through BLI is the reduction in fluid power required for generating a given amount of thrust, i.e. velocity differential. For a fuselage boundary layer as depicted in Fig. 2, the thrust generated is indicated as the difference of the velocity profiles with and without the propulsor. The energy required to fill in the wake momentum deficit is lower than what is needed to create excess velocity. The potential saving can be expressed with the Power-Saving Coefficient (PSC) [6]

$$\mathrm{PSC} = \frac{P_{\mathrm{NoBLI}} - P_{\mathrm{BLI}}}{P_{\mathrm{NoBLI}}} \qquad (1)$$

where P_{NoBLI} denotes the power required by a conventional non-ingesting propulsion system contrary to the P_{BLI} required by an ingesting system to achieve a drag-thrust equilibrium.

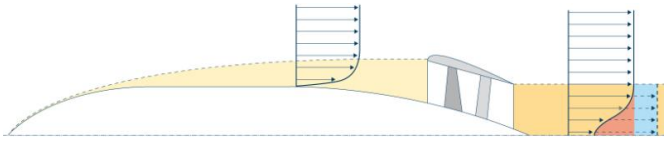

Fig. 2: Schematic of the filling of the fuselage momentum deficit in the wake for a Propulsive-Fuselage configuration [7].

The fuselage boundary layer provides a particularly worthwhile target for BLI since it concentrates up to half of the viscous drag for a passenger aircraft application [7]. The long

drawn-out cylindrical shape of the fuselage results in large radial dimensions of the boundary layer, allowing for considerable blade heights of the propulsor. Although the pressure drag created by the wake constitutes only a small share of the overall drag of a fuselage, it can be diminished additionally by virtue of the regeneration of the boundary layer.

In recent studies, the potential benefits of BLI have been addressed [4,6-12]. A PSC of 9.4% (for the complete aircraft) relative to the non-BLI reference case has been calculated in an initial assessment utilizing displacement thickness of the fuselage boundary layer and assuming perfect wake filling [4]. Advanced studies that incorporated aircraft integration effects showed up to 10% of power saving potential [7] and improvements of block Energy Specific Air Range (ESAR) up to 9.9% [8]. Another study by utilizing several methods of differing fidelity gave a PSC of 3-4% [9]. A further study with Computational Fluid Dynamics (CFD) resulted in a power saving of up to 11%; however, a decline in total power saving up to -16% was determined due to deterioration in inlet pressure recovery in a non-optimized engine setup [10]. In an earlier study by Ref. [11] assessing the benefit of an unducted fuselage fan at aircraft level, a benefit of 4-6% was described.

In the five last years, ONERA has conducted a theoretical study of BLI on a simple axisymmetric configuration using CFD, with a nacelle downstream a fuselage [12]. First, the real engine at transonic flight conditions was simulated using a mass flow rate condition in the fan plane and in the turbine plane with a total temperature condition in the turbine plane. Then, wind tunnel tests were been performed at low speed on a similar configuration where the real engine inside the nacelle was replaced by a fan driven by an electric engine, and the fan was simulated by an actuator disk using CFD. The theoretical study proved substantial power saving could be obtained through BLI, and the wind tunnel tests demonstrated that the theoretical approach was appropriate.

In this paper, a number of quasi-analytical methods are presented that allow covering a broad design space with regards to Propulsive-Fuselage architectures. Thereto, this paper is part of the ongoing work on the European Comission funded Framework Programme 7 Level-0 research project DisPURSAL [13] about Distributed Multiple-Fans and Propulsive-Fuselage concepts.

2 Book-keeping Standard for Boundary Layer Ingestion

It is important to assess the benefits through BLI consistently because changes in propulsion system inlet total pressure, fuselage drag and propulsive efficiency have to be factored into the overall result. In fact, the friction drag of the fuselage increases compared to the conventional fuselage due to localized flow acceleration by the propulsor and boundary layer regeneration. Also, the propulsion system is impaired by non-uniform and potentially disturbed inlet flow, and a lower inlet total pressure compared to a podded engine in the freestream. These disadvantages need to be compensated by an improved propulsive efficiency.

The net thrust, T_{N}, is used as a parameter to account for the change in drag, D,

$$T_{\mathrm{N}} = T - D \tag{2}$$

where T denotes the gross thrust produced by the propulsor. The parameter T is obtained through integration across the propulsor radius, r_{prop}, with a momentum balance

$$T = 2\pi \cdot \int_{r_{\mathrm{prop}}} [\Delta p + \Delta(\rho U^2)] \cdot r \, dr \tag{3}$$

with Δ denoting the change in fluid state (pressure and density) across the propulsor. The fuselage drag, D, is obtained as the sum of friction drag, D_f, and pressure drag, D_p. The parameter D_f is calculated as the integral of wall shear stress along the fuselage surface. For a fuselage without propulsor, D_p is obtained as the product of the displacement area of the fuselage and the freestream dynamic head [14]. The pressure drag decreases under presence of a propulsor due to wake filling. This is modelled by assuming the pressure drag decreases

linearly with net thrust T_N until it is zero. For higher net thrusts, the pressure drag is assumed to be zero.

The PSC is usually related to the overall propulsion system power required to propel the aircraft. Here, in contrast, the fluid power introduced into the flow is compared to the power required to create the same thrust for a podded engine in the free stream ingesting the same mass flow, $\dot{m}$, as the Propulsive-Fuselage.

$$P_{\mathrm{noBLI}} = \dot{m} \cdot \frac{1}{2}\Delta(U^2) \qquad (4)$$

where the velocity difference, ΔU, is obtained by

$$\Delta U = \frac{T}{\dot{m}} \qquad (5)$$

Since the propulsion system is out of the scope of this paper, effects emerging from changes in propulsion system efficiency or weight are not covered. Moreover, cascade effects emanating from the concept such as component and structural weight implications and aerodynamic changes are not considered. This would be necessary for an integrated assessment of the Propulsive-Fuselage concept.

3 Quasi-Analytical Aerodynamic Methods for Propulsive Fuselages

In the conceptual stage of aircraft design, it is important to be able to cover a large design space with sufficient fidelity. Methods that were used in the past were not able to provide both of these two requirements. Simple methods based on flat plate theory provide fast computation, but lack sufficient fidelity because they are not applicable for accounting the presence of pressure gradients or a propulsor. High fidelity CFD methods, however, can only cover a very limited design space due to computational effort. Therefore, a method based on analytical relations has been developed that is capable of including the pressure gradient along the fuselage, the turbulent boundary layer, and the impact of the propulsor on the boundary layer and the pressure gradient.

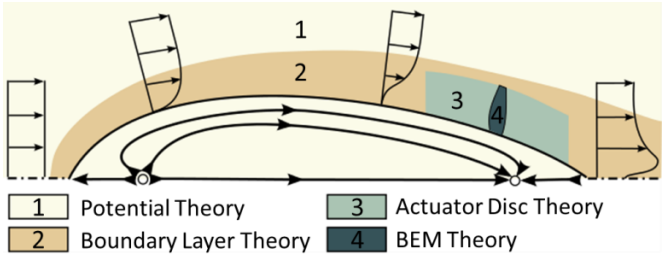

Fig. 3: Schematic of the Fuselage with fluid flow and regions indicating the application of: (1) Potential Theory; (2) Compressible Boundary Layer Theory; (3) Compressible Actuator Disc Theory; and, (4) Blade Element Momentum (BEM) Theory.

The methods required to represent these effects are displayed schematically in Fig. 3 (above) indicating the regions where they are applied. First, Potential Theory is used to obtain the pressure gradient along the fuselage contour. Here, the fuselage contour is approximated by means of a finite number of sinks and sources along the axis of revolution. Second, the boundary layer is calculated with compressible, turbulent Boundary Layer Equations for axisymmetric bodies. Finally, the impact of the propulsor on the boundary layer is modelled with Compressible Actuator Disc Theory and Blade Element Momentum (BEM) theory. The first is required to get effects on the boundary layer upstream and downstream of the propulsor as indicated in Fig. 3, “region 3”, while the second is necessary to obtain a realistic radial work distribution across the propulsor. The implementation is described in detail in the following.

3.1 Pressure Distribution on a Fuselage

The pressure gradient in the boundary layer is imposed by the outer, irrotational flow. For an irrotational flow, the velocity vector, $\boldsymbol{U}$, can be expressed as the gradient of a potential function, Φ [15].

An incompressible flow follows a Laplace equation, which has several solutions, called elementary solutions. To obtain the pressure

distribution of an axisymmetric body of revolution such as a fuselage, these elementary solutions of the Potential Theory can be used. The modelling is done according to Ref. [16] with a distribution of 3D sources and sinks placed on the symmetry axis of the body at the axial displacement, x_0. The potential function for this model in Cartesian coordinates is

$$\Phi(x,y,z) = \frac{1}{4\pi}\int_0^L \frac{q(x)}{\sqrt{(x-x_0)^2+y^2+z^2}}dx \qquad (6)$$

with x being the coordinate in direction of the symmetry axis and $q(x)$ being the source and sink distribution.

This function is a Fredholm integral equation, which has no analytical solution for $q(x)$. Therefore, the source and sink distribution is solved iteratively for finite sinks and sources using the non-linear Levenberg-Marquardt algorithm. Start values for this problem can be obtained via an approximation for thin bodies of revolution which have a small velocity difference between the fuselage surface velocity and the undisturbed free stream velocity [17].

An approximation of the source and sink distribution is obtained with

$$Q(x) = U_\infty \pi \frac{dR^2}{dx} \qquad (7)$$

with R being the fuselage radius at x. With the distribution and the velocity difference, ΔU, obtained through the source distribution, $Q(x)$, a second order approximation can be calculated iteratively with

$$Q(x) = \pi \frac{d}{dx}[R^2\,(U_\infty + \Delta U)] \qquad (8)$$

and a suitable initial solution for the source strength distribution can be obtained iteratively in this manner with convergence after 5 loops.

In Fig. 4, the streamlines obtained with the above mentioned approximation and the source and sink distribution are shown. The thick dashed line indicates the fuselage geometry, the solid line indicates the solution for the fuselage streamline of the starting values, and the dots on the x-axes indicate the location of the discrete sources and sinks. As can be seen the sources and sinks and the target points are not uniformly distributed along the x-axis. The density is higher in regions of large fuselage radius variation to increase the quality of the result.

The resulting incompressible pressure distribution of the clean fuselage is transformed into the compressible pressure distribution using the Prandtl-Glauert-Ackeret correction for bodies of revolution. Prior to calculating the pressure coefficient, a geometric transformation is applied to the thickness ratio

$$\frac{R'}{L} = \sqrt{|1-M^2|}\frac{R}{L} \qquad (9)$$

where L is the fuselage length and R' is the transformed radius.

The pressure gradient obtained for the transformed geometry is then transformed into the compressible pressure gradient using

$$c_P = \frac{c_P{}'}{|1-M^2|} \qquad (10)$$

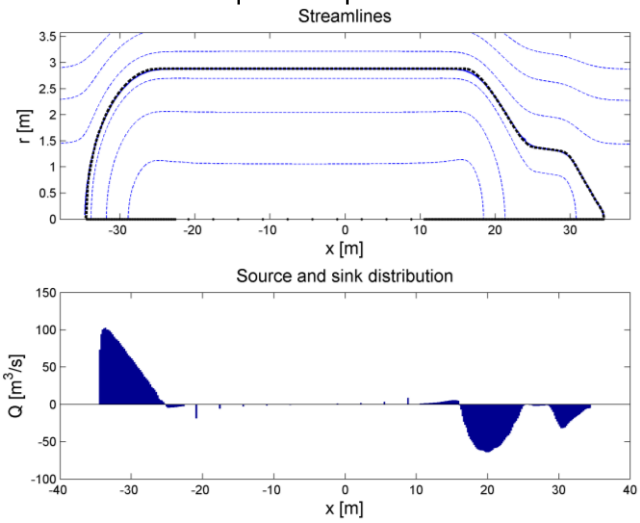

Fig. 4: (top) Streamlines with discrete source (black dots) and fuselage surface (black dashed line) and (bottom) source distribution $Q(x)$ for a Propulsive-Fuselage geometry after 5 iteration loops.

3.2 Simulation of a Compressible Turbulent Boundary Layer with Pressure Gradient

The change of the flow variables for velocity, U and V, density, ρ, and the total enthalpy, H, in the boundary layer of the Propulsive-Fuselage is calculated with the boundary layer equations for an axisymmetric body according to Ref. [18] along the arc length, s. The following equations constitute the balance for mass

$$\frac{\partial(r\rho U)}{\partial s} + \frac{\partial(r\rho V)}{\partial y} = 0 \tag{11}$$

momentum in the s direction

$$\rho U\frac{\partial U}{\partial s} + \rho V\frac{\partial U}{\partial y} = -\frac{\partial p}{\partial s} + \frac{1}{r}\frac{\partial}{\partial y}\left(r\rho(\nu + \nu_t)\frac{\partial U}{\partial y}\right) \tag{12}$$

and energy

$$\rho U\frac{\partial H}{\partial s} + \rho V\frac{\partial H}{\partial y} = \frac{1}{r}\frac{\partial}{\partial y}\left(r(U\tau - q)\frac{\partial U}{\partial y}\right) \tag{13}$$

Here, r denotes the radius, ν the kinematic viscosity, ν_t the turbulent kinematic viscosity, τ the shear stress term and q the heat conductance term. The consideration of surface curvature radii is not required for typical fuselage geometries as long as the radii are larger than the boundary layer thickness.

Equations (12) and (13) were solved for the gradient of U and H in the s direction, respectively. Subsequently, the differential equation was solved numerically with an adaptive step size ordinary differential equation solver. The equation for mass balance (11) was used to obtain V with

$$V(y) = -\int_0^y \left(\frac{1}{r\rho}\frac{\partial(r\rho U)}{\partial s} + \frac{V}{\rho}\frac{\partial \rho}{\partial y} + \frac{V}{r}\frac{\partial r}{\partial y}\right)\partial y \tag{14}$$

The density was calculated using the equation of state, assuming a constant heat capacity, $\bar{c_p}$, with

$$\rho = \frac{p\bar{c_p}}{R_g\left(H - \frac{|\boldsymbol{U}|^2}{2}\right)} \tag{15}$$

with R_g being the specific gas constant.

This approach allows for a grid-free solution of the boundary layer equations and, therefore, a minimized effort for grid generation. In the wall normal direction, y, the flow variables are discretized by means of non-equidistant cells. The wall normal size of the cell closest to the wall is defined to have a dimensionless distance, $y^+ = 1$, for an equivalent flat plat turbulent flow in order to resolve the laminar sub-layer [19]. The parameter y^+ is defined by

$$y^+ = \frac{y}{\nu}\cdot\sqrt{\frac{\rho}{\tau_0}} \tag{16}$$

with the wall shear stress, τ_0, estimated according to Ref. [15] for a flat plate with the same arc length.

The cells, then, grow in wall normal direction, r, with an exponential stretching factor of 1.05. This allows for a sufficient resolution of the complete boundary layer including the laminar sub-layer, while maintaining a reasonably small number of cells [20]. The gradients in wall normal direction for the non-equidistant cells were computed with central gradients of second order according to Ref. [19].

The turbulent kinematic viscosity, ν_t, was calculated by means of a wall-gradient based zero equation model based on turbulent mixing length. Since the laminar sub-layer is resolved, no wall function needs to be provided in the model. The turbulent mixing length, l_m, was calculated according to Ref. [21] with

$$l_m = \min(\kappa y, 0.085\cdot\delta_{99})\cdot\left(1 - \exp\left(-\frac{y^+}{A^+}\right)\right) \tag{17}$$

where $\kappa = 0.41$ is an empirical constant describing the intensity of the turbulence close to the wall, δ_{99} is the boundary layer thickness where 99% of the freestream velocity at this arc length, u_e, is reached, and $A^+ = 26$ is an empirical constant describing the attenuation of turbulence far from the wall. The turbulent kinematic viscosity is then obtained via

$$\nu_t = l_m^2 \cdot \left|\frac{\partial U}{\partial y}\right| \qquad (18)$$

The turbulence model according to Ref. [22] was selected because it yielded the best agreement with CFD results by Ref. [10] with regards to boundary layer displacement thickness, δ, and momentum loss thickness, θ, as depicted in Fig. 5 (overleaf). The error calculated as the average of three stations at the axial lengths, $\frac{x}{L} = 0.70$, 0.75 and 0.80, was -5.1% for the displacement thickness, δ, +5.7% for the momentum loss thickness, θ, and +8.0% for the energy loss thickness, θ^* (not displayed in the figure). The general trends with arc length agree very well for both parameters. It is highlighted that the laminar sub-layer was not resolved in CFD and a wall function was used instead which may explain the error observed.

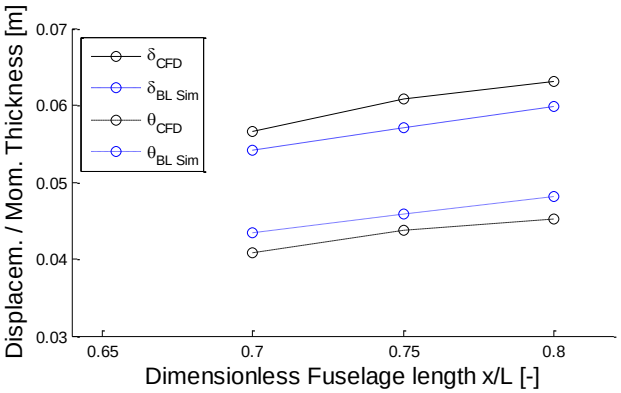

Fig. 5: Validation results of displacement thickness, δ^*, and momentum loss thickness, θ, of the implemented turbulence model against CFD results [10] for a simple fuselage geometry.

3.3 Compressible Actuator Disc Theory

The propulsor has been modelled using the actuator disc simplification. Thereto, the propulsor is lumped into a single disc with no axial dimension. The effect of the propulsor is then obtained by assuming a uniform pressure difference, Δp, across the disc, implicitly given by a momentum balance around the propulsor and the thrust, T, created by the propulsor. The static pressure in front and aft of the propulsor is then obtained via Compressible Actuator Disk Theory according to Ref. [22]. In the present context, the theory has been adapted to incorporate different inlet and outlet static pressures, and to allow for a radial work distribution across the propulsor, thus, deviating from the uniform pressure difference.

For the solution of the actuator disc problem, the fluid state at inlet and outlet are denoted by 0 and 3, respectively, and in front of and aft of the disc with 1 and 2, respectively. For the solution of all 10 unknowns (U_1, U_2, U_3, ρ_1, ρ_2, ρ_3, A_0, A_3, p_1, p_2), the equations for continuity for $0 \rightarrow 1$, $1 \rightarrow 2$ and $2 \rightarrow 3$, momentum conservation for $1 \rightarrow 2$ and $0 \rightarrow 3$, isentropic relation for $0 \rightarrow 1$ and $2 \rightarrow 3$, total pressure conservation for $0 \rightarrow 1$ and $2 \rightarrow 3$ as well as the energy equation considering the total enthalpy added for $0 \rightarrow 3$ need to be satisfied. With this approach, the actuator disc problem can be solved until the Mach number in front of the propulsor, M_1, becomes greater than 1. The results for pressure and velocities for all four stations in dependence of thrust per area for the case of equal far-field inlet and outlet pressure are depicted in Fig. 6. It can be seen that the velocity is highest in front of the propulsor and lowest aft of the propulsor.

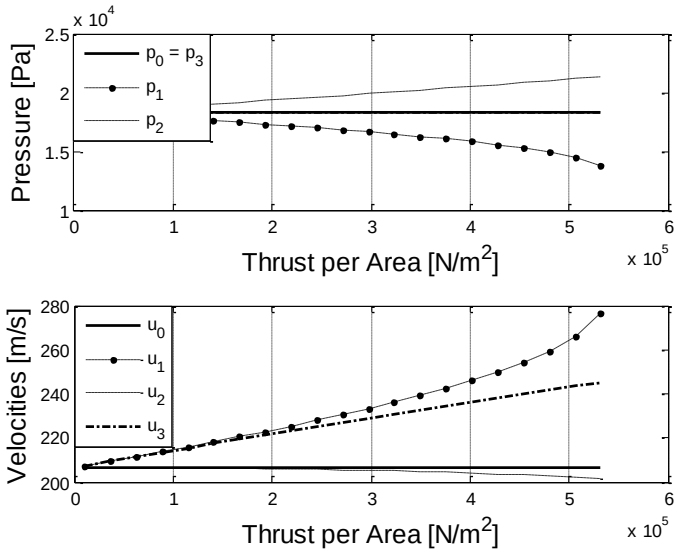

Fig. 6: Pressure (top) and velocity (bottom) of inlet (0) and outlet (3) conditions as well as in front of (1) and aft of (2) an actuator disc for compressible conditions and different thrust per area.

The far-field inlet and outlet conditions for the Compressible Actuator Disk Theory as well as the pressure gradient upstream and downstream of the propulsor are obtained by representing the disc as a disc of doublets according to Ref. [23], which yields

$$\Delta p(x^*) = \frac{\Delta p}{2}\left(1 - \frac{x^*}{\sqrt{R_{\text{tip}}^2 + x^{*2}}}\right) \qquad (19)$$

with x^* being the distance upstream or downstream of the actuator disc and R_{tip} being the radius of the propulsor. When considering a distance of two times the blade height upstream and downstream from the propulsor plane, the solution of Ref. [23] has a relative error of 5.0% from the far-field conditions. Therefore, the static pressures according to Potential Theory at these points have been selected as boundary conditions for the actuator disc inlet and outlet conditions. The correction for a non-uniform pressure ratio, and thus, work distribution across the propulsor is explained in the following section about propeller modelling.

3.4 Propeller Modelling with Blade Element Momentum (BEM) Theory

The calculation of the radial, induced velocity profile by the propeller is based on the BEM Theory originally developed in Ref. [24]. This is a frequently used hybridization of the Actuator Disk Theory and the Blade Element Theory [25]. While the first method assumes the pressure rise of the propeller to be uniform across the actuator disk, and thus, neglects the non-uniform pressure distribution of blades, the latter one regards the propeller blade as a twisted wing using a spanwise discretization, each element being aerodynamically independent from another. The coupling of these two approaches allows for the determination of the propeller performance including the aerodynamic forces imposed on the propeller as well as the induced velocities near the rotor. As opposed to the aforementioned theories, it simultaneously captures the effects of compressibility and viscous losses, hence yielding a better accuracy than using both theories separately.

A methodic approach to a practical employment of BEM theory for the design of propellers was proposed by Ref. [26] and adjusted to allow for a radial inlet velocity profile at the propeller face imposed by the boundary layer. As in the simplified Blade Element Theory, each blade is divided into a finite numbers of elements of which each is considered as a separate 2D airfoil. Applying momentum conservation laws and equilibrium of forces acting on each blade together with a radial twist distribution, the local angle of attack for each element is obtained.

In order to calculate lift and drag coefficients, the method was supplemented with the characteristics of a NACA airfoil. Due to the large amount of experimental and analytical information available in literature, data of a NACA 16-series airfoil frequently used for propeller applications by Ref. [27] were employed. The spanwise distribution of blade twist and chord length were implemented according to Ref. [29], which was considered suitable for the present application, as extensive

experimental data for freestream Mach numbers up to M0.73 were available.

Using this, an iterative procedure was implemented yielding the spanwise distribution of induced velocities in axial and tangential directions. Through radial integration, propeller performance metrics such as thrust and torque coefficients as well as propeller efficiency are obtained. While experimentally derived airfoil data includes the influence of compressibility and viscosity, 3D effects are ignored. Hence, a correction factor, F, to the induced velocity field as derived by Ref. [24] was introduced into the model in order to account for tip effects not captured in two-dimensional airfoil theory:

$$F = \frac{2}{\pi}\arccos[\exp(-f)] \qquad (20)$$

with

$$f = \frac{B}{2}\frac{1-x}{\sin\phi_t} \qquad (21)$$

including sensitivity to the number of blades, B, the relative spanwise blade coordinate with respect to the propeller tip radius, $x = r/R_{tip}$, and the flow angle at the blade tip, ϕ_t. Effects emanating from design deviations for hub to tip ratios larger than those of conventional propellers were neglected.

The model was validated against experimental results published in Ref. [29]. The propeller efficiency calculated as a function of advance ratio, $J = U_\infty/(2nR_{tip})$, is depicted in Fig. 7 (overleaf), where V is the free stream velocity at that point according to potential theory, and n the rotational speed of the propeller. As can be seen from Fig. 7, the model slightly overestimates efficiency which may be attributed to the relatively simple tip loss correction. The error of the calculation is within a $\pm 5\%$ range. According to Ref. [24], accuracy of the BEM theory increases with the number of blades. Therefore, less deviation may be expected for the application considered with a significantly higher blade count.

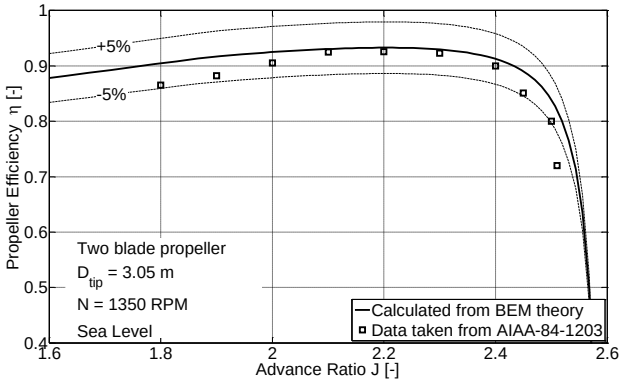

Fig. 7: Results for propeller efficiency, η, against advance ratio, J, for the propeller model compared to reference data.

The tangential velocity components of the flow behind the propeller, i.e. the swirl created by the propeller, have been neglected for the course of these studies. This can be achieved either with a rotor stator combination or with a counter-rotating propeller installation. This is then lumped into a single propeller without swirl. If only a single propeller is present, the swirl downstream of the propeller would have to be considered additionally in 3D boundary layer equations.

The development of the axial pressure according to Actuator Disc Theory and Potential Theory is corrected by the radial work distribution obtained via BEM theory. The pressure gradient is then multiplied with a normalized radial work ratio

$$w(r) = \frac{(U_3^2 - U_0^2)\cdot\int_r U_1\cdot r\cdot \mathrm{d}r}{\int_r (U_3^2 - U_0^2)\cdot U_1\cdot r\cdot \mathrm{d}r} \qquad (22)$$

with U_0 and U_3 being the far field inlet and outlet radial velocity profiles in the axial direction, respectively, and U_1 being the radial velocity profile in the propeller plane.

4 High-Fidelity Propulsive-Fuselage Analysis

Two different CFD methods are available at ONERA to simulate the aerodynamics of a Propulsive-Fuselage.

4.1 Accurate Version of an Actuator Disk

For the Propulsive-Fuselage concept analysis, ONERA used its elsA CFD software [29] solving RANS equations. Computations were performed on an axisymmetric configuration in order to simplify the meshing process. The engine includes a fan with its stator. A stator cannot be easily simulated with an actuator disk condition, so the fan and its stator were simulated using two counter-rotating actuator disk conditions.

That actuator disk condition needs a disk model giving radial distributions of the pressure ratio, of the temperature ratio and of the tangential flow deviation for several mass-flow rates. Building a disk model without knowing other information than the fan diameter and its angular velocity is a real challenge. The tangential flow deviation must be realistic, otherwise flow separation may occur.

The disk models were built using the simple Glauert Theory for propellers in an incompressible freestream [24]. This theory gives an equation linking the axial velocity induced in the disk plane and the tangential induced velocity downstream the disk plane. The solution corresponding to a given freestream M and to a given mass-flow rate is found by coupling the theory with Blade Element Theory where the lift coefficient of a blade element is assumed to be proportional to the local aerodynamic angle of attack. An iterative process is conducted on the tangential induced velocity until Glauert Theory and Blade Element Theory give the same propeller thrust.

Finally, for a given total pressure and a given total temperature, only three parameters are needed to build a disk model: (1) propeller angular velocity; (2) freestream M; and, the mass-flow rate that can be given through an average M in the disk plane. In addition, an assumption should be made on the radial distribution of the pressure ratio: here, the radial distribution of the local propulsive efficiency factor is assumed to be constant, as this leads to a maximum global propulsive efficiency according to Glauert.

For the maximum propeller angular velocity, freestream and disk plane M are chosen according to the constraints of the Glauert Theory such that they give the maximum thrust. This allows defining a simple blade geometry that can be used to compute the propeller at other conditions. The Fig. 8 shows the result of a computation with two counter-rotating actuator disks.

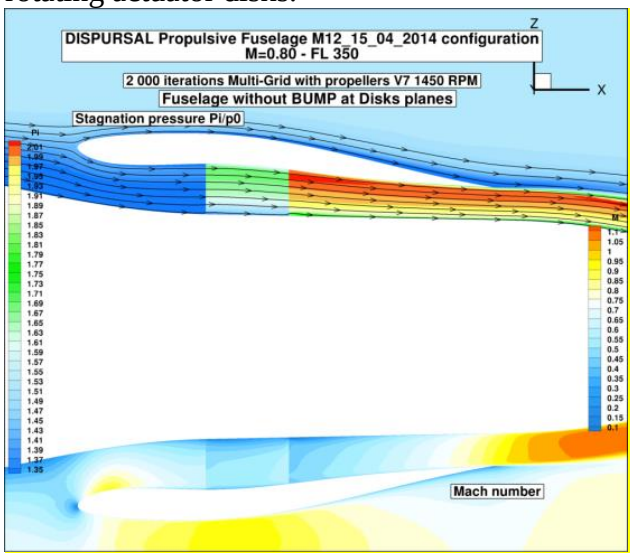

Fig. 8: Propulsive-Fuselage CFD result with two actuator disks.

The thrust of each disk is the difference between the dynalpy fluxes downstream and upstream the disk. The injected power is the difference between the total enthalpy flux downstream of the second disk and upstream of the first disk. The configuration drag is computed by integrating pressure and skin friction over the fuselage skin and over the nacelle skin. Results from computations for several propeller angular velocities allow building a curve showing the injected power as a function of the resulting axial force over the configuration. The PSC defined above cannot be computed since no results for a reference configuration without BLI exists, but one can compare several BLI configurations and determine the best geometry for a desired thrust range.

This kind of actuator disk is able to adapt itself to the incoming flow conditions. Therefore, it is well suited for BLI purposes, especially for the accurate prediction of the performance of a Propulsive-Fuselage.

4.2 Simpler Version of an Actuator Disk

Another way to simulate the fan effect involves using a simpler version of the actuator disk. That version introduces surface forces, i.e. homogeneous to a pressure jump, into the elsA CFD code [29] on the boundary condition. The force can either be a constant value, or a file containing a map of local forces. Forces can be added along the x, y and z axes in any possible combination, provided it is consistent with the laws of physics.

Such an example is illustrated in Fig. 9, where a field of the coefficient of total pressure is plotted. In this case, a constant axial surface force of $5\,000\,\frac{\mathrm{N}}{\mathrm{m}^2} = 5\,000$ Pa is applied on the whole actuator disk boundary condition. By axial it means along x, or more precisely, perpendicular to the actuator disk.

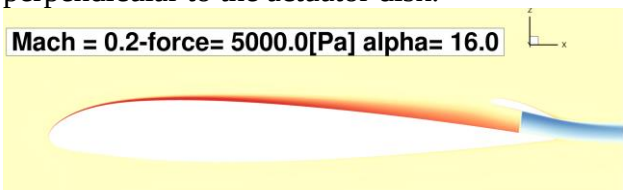

Fig. 9: A simple actuator disk on a 2D configuration (total pressure is plotted).

The loss of total pressure in the boundary layer can easily be seen in red, and the actuator effect is highlighted in the blue area downstream of the actuator disk boundary condition. Note that the boundary layer crosses the condition and exits in white and not in blue, showing that the boundary layer has been re-energized by the actuator as expected.

The main advantage of this condition with respect to the other one is that no swirl is needed. Therefore, this condition can be used in 2D longitudinal configurations, which is not possible with the other one. Nevertheless, using that condition with no swirl means that the physics is simplified. Moreover, no losses are modeled through this condition, it is considered to be an isentropic compression. Therefore, any performance assessment must be done so keeping in mind it provides an optimistic estimate of the potential performance savings. It is, nonetheless, a very convenient and easy to use boundary condition, perfectly suitable for such parametric studies.

5 Application of Aerodynamic Methods to a Propulsive-Fuselage Geometry

The methods presented in the previous section have been applied to a fuselage geometry that is presented in Fig. 10. The propulsor is located after a contraction from the fuselage diameter. This shape leads to a widening of the boundary layer upstream of the propulsor and, thus, allows achieving reasonable hub-to-tip ratios of about 0.7 as well as limiting tip velocities.

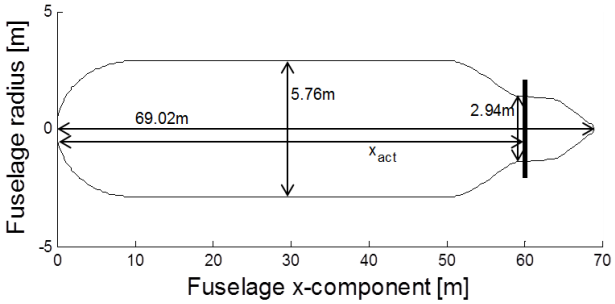

Fig. 10: Profile of the fuselage geometry with important dimensions (not scaled equally).

The boundary conditions were set to typical cruise conditions with a flight altitude of 35000 ft and a free stream Mach number of M0.75. The fuselage maximum vertical diameter is 5.76 m and the fuselage length is 69.0 m in order to allow room for 340 PAX. The actuator disc was placed at $x_{\mathrm{act}} = 58.5$ m. The blade height is 0.62 m, giving a propeller diameter of 4.19 m.

Due to the relatively high freestream Mach number for the propeller of M0.75, the disk loading is limited by M1.00 in front of the propulsor yielding a maximum gross thrust $T = 15.0$ kN for the quasi-analytical methods. The results for resulting drag, D, net thrust, T_N, and Power Saving Coefficient, PSC, as well as other figures of merit are listed in Table 1 (overleaf).

The results in the investigated configuration indicate that it is not possible to achieve a positive net thrust, T_N, for a single propeller configuration with the given propeller area. The pressure drag, D_p, does reduce linearly with net thrust, T_{N}, but does not diminish entirely. The friction drag, D_f, increases slightly as the boundary layer is accelerated and regenerated around the

propulsor. The power, P, added to the fluid increases more than proportionally when the propulsor exit velocity increases. Consequently, the PSC is reduced at higher thrust levels.

Table 1: Results for a range of disc loadings.

T [kN]	0	5	10	15
$\frac{T}{A}\left[\frac{N}{m^2}\right]$	0	719	1439	2158
D_f [kN]	19.36	19.51	19.69	19.85
D_p [kN]	3.31	2.48	1.66	0.80
D [kN]	22.67	21.99	21.35	20.65
T_N [kN]	-22.67	-16.99	-11.35	-5.65
P [kW]	-	785.3	1669.6	2621.7
PSC [%]	-	31.2	28.6	26.8
$\frac{p_{t,2}}{p_{t,1}}$ [−]	-	1.025	1.051	1.078
$\dot{m}\left[\frac{kg}{s}\right]$	-	418.0	440.5	461.5
η_{pr} [−]	-	1.416	1.332	1.272

The boundary layer thickness at the propulsor is approximately $\delta_{99} = 0.88$ m which suggests that the propulsor is completely immersed in the boundary layer. Combined with the low pressure ratio across the propulsor, this allows for propulsive efficiencies greater than 1.00. The effect decreases with increasing propulsor pressure ratio. This is only possible when fluid of velocity lower than the free stream velocity U_∞ is accelerated.

The results for the quasi-analytical method and the CFD by ONERA are plotted in Fig. 11 (overleaf), showing results for the power injected by a propulsor, P, versus net thrust, T_N. For the ducted fan, a positive net thrust, T_N, was achieved since it was not limited by the propeller inlet M. The results indicate good agreement for the drag of the unpropelled fuselage, but a difference in slope for the applied propeller of 9.1% arose. A major reason for this difference may be found in the use of a propeller for the quasi-analytical methods and the use of a ducted fan for the CFD in the presence of a nacelle. Also, a quadratic fit might not represent the non-linear characteristic of a ducted fan well enough.

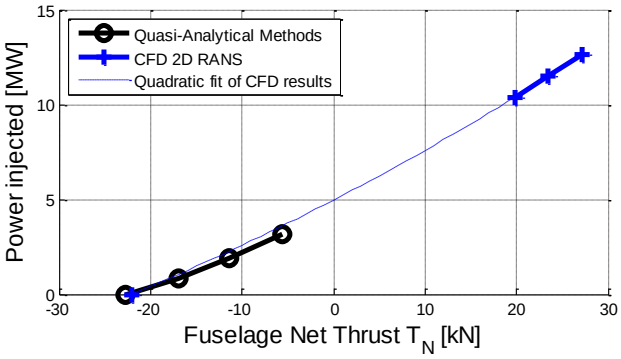

Fig. 11: Plot of the results for power injected, P, vs. net thrust generated, T_N, obtained by quasi-analytical methods and by 2D RANS CFD.

6 Conclusion

The quasi-analytical methods presented have been verified individually and compared to Computational Fluid Dynamics (CFD) results in order to validate interfacing between the methods. The conjoint results have been shown to provide reasonable results for a configuration like the Propulsive Fuselage. In order to increase applicability of the quasi-analytical methods in exploring the design space, the implementation of further propulsor configurations is necessary. This includes ducted fans to allow going to higher Mach numbers and to represent the fuselage impact, and two-stage configurations, i.e. counter-rotating propellers and ducted counter-rotating fans, to increase the overall pressure ratio and, thus, net thrust. All of these configurations can be represented by the applied Actuator Disc Theory. The results have shown that a Propulsive Fuselage configuration can provide large savings. The relative power savings, expressed by the Power Saving Coefficient, are highest for low levels of thrust. The absolute power saving does, however, increase even at higher thrust levels with positive net thrust.

7 Acknowledgement

The research leading to results presented in this paper has received funding from the European Commission Seventh Framework Programme (FP7) through the DisPURSAL Project under Grant Agreement No. 323013.

References

[1] Kim HD. *Distributed propulsion vehicles*. *27th International Congress of the Aeronautical Sciences*. Nice, France, 2010.

[2] Yaros S, Sexstone M, Huebner L. *Synergistic airframe-propulsion interactions and integrations*. NASA/TM-1998-207644, 1998.

[3] Gohardani AS, Doulgeris G, Singh R. *Challenges of future aircraft propulsion: A review of distributed propulsion technology and its potential application for the all electric commercial aircraft*. Prog. Aerosp. Sci. 47, 369–391, 2011.

[4] Steiner H, Seitz A, Wieczorek K, Plötner K, Isikveren AT, Hornung M. *Multi-Disciplinary Design and Feasibility Study of Distributed Propulsion Systems*. *28th International Congress of the Aeronautical Sciences*. Brisbane, Australia, 2012.

[5] Isikveren AT, Seitz A, Bijewitz J, Hornung M, Mirzoyan A, Isyanov A, van Toor J, Stückl S. *Recent Advances in Airframe-Propulsion Concepts with Distributed Propulsion*. *29th International Congress of the Aeronautical Sciences*. Paper 1.7.3, St Petersburg, Russia, 2014. (to be published)

[6] Smith LH. *Wake Ingestion Propulsion Benefit*. J. Propuls. Power. 9, 74–82, 1993.

[7] Seitz A, Gologan C. *Parametric Design Studies for Propulsive Fuselage Aircraft Concepts*. *4th CEAS Air & Space Conference*. Linköping, 2013.

[8] Seitz A, Bijewitz J, Kaiser S, Wortmann G. *Conceptual Investigation of a Propulsive Fuselage Aircraft Layout*. Aircr. Eng. Aerosp. Technol. J. 2014. (to be published)

[9] Plas A. *Performance of a Boundary Layer Ingesting Propulsion System*, Master's Thesis, Massachusetts Institute of Technology, 2006.

[10] Van Dyck L. *Aerodynamic Analysis and Design Study of a Boundary Layer Ingesting Propulsive Fuselage Concept using OpenFOAM*. 2012.

[11] Bolonkin A. *A high efficiency fuselage propeller (Fusefan) for subsonic aircraft*. SAE Trans. 1999.

[12] Atinault O, Carrier G, Grenon R, Verbecke C, Viscat P. *Numerical and Experimental Aerodynamic Investigations of Boundary Layer Ingestion for Improving Propulsion Efficiency of Future Air Transport*. *31st AIAA Applied Aerodynamics Conference*. San Diego, CA, 2013.

[13] Isikveren AT (Bauhaus Luftfahrt e.V.), *Distributed Propulsion and Ultra-high By-pass Rotor Study at Aircraft Level (DisPURSAL)*. FP7-AAT-2012-RTD-L0, Proposal No. 323013, European Commission Directorate General for Research and Innovation, 14 March 2012.

[14] Drela M. *Flight Vehicle Aerodynamics*. The MIT Press, Boston, 2014.

[15] Schlichting H, Gersten K. *Boundary-layer theory*. Springer, New York, 2000.

[16] Fuhrmann G. *Theoretische und experimentelle Untersuchungen an Ballonmodellen*, Dissertation, Georg-August-Universität zu Göttingen, 1912.

[17] Schlichting H, Truckenbrodt E. *Aerodynamik des Flugzeugs. 2. Band*. Springer, Berlin, Heidelberg, 1969.

[18] Cebeci T, Smith AMO, Mosinskis G. *Calculation of Compressible Adiabatic Turbulent Boundary Layers*. AIAA J. 8, 1974–1982, 1974.

[19] Ferziger JH, Perić M. *Computational Methods for Fluid Dynamics*. Springer, Berlin, Heidelberg, 2002.

[20] Nichols RH. *Turbulence Models and Their Application to Complex Flows*. University of Alabama at Birmingham, 2010.

[21] Van Driest ER. *On Turbulent Flow Near a Wall*. J. Aeronaut. Sci. (Institute Aeronaut. Sci.) 23, 1007–1011, 1956.

[22] Vogeley A. *Axial-Momentum Theory for Propellers in Compressible Flow*. NACA Technical Note 2164, 1951.

[23] Veldhuis L. *Propeller wing aerodynamic interference*, Doctoral Thesis, Delft University of Technology, 2005.

[24] Glauert H. *Airplane propellers*. Springer, Berlin, 1935.

[25] Rwigema M. *Propeller blade element momentum theory with vortex wake deflection*. *Proceedings of the 27th Congress of the International Council of the Aeronautical Sciences*. Nice, France, 2010.

[26] Adkins CN, Liebeck RH. *Design of optimum propellers*. J. Propuls. Power. 10, 676–682, 1994.

[27] Abbott IH, Von Doenhoff AE, Stivers LJ. *Summary of Airfoil Data*. NACA Report No. 824, 1945.

[28] Chang L, Stefko G. *Application of an optimization method to high performance propeller designs*. *20th Joint Propulsion Conference*. Cincinnati, Ohio, 1984.

[29] Cambier L, Heib S, Plot S. *The Onera elsA CFD software: input from research and feedback from industry*. Mech. Ind. 14, 159–174, 2013.

8 Contact Author Email Address

sascha.kaiser@bauhaus-luftfahrt.com
olivier.atinault@onera.fr

9 Copyright Statement